Basin Research
February 2022, Volume 34 Issue 1 Pages 321-341
https://doi.org/10.1111/bre.12621
https://archimer.ifremer.fr/doc/00865/97721/

Archimer
https://archimer.ifremer.fr

Assessing the rate of crustal extension by 2D sequential restoration analysis: A case study from the active portion of the Malta Escarpment

Gambino Salvatore [1,*], Barreca Giovanni [1,2], Gross Felix [3,4], Monaco Carmelo [1,2,5], Gutscher Marc-Andre [6], Alsop G. Ian [7]

[1] Department of Biological, Geological and Environment Sciences, University of Catania, Catania, Italy
[2] CRUST—Interuniversity Center for 3D Seismotectonics with Territorial Applications, Chieti, Italy
[3] Institute of Geosciences, Kiel University, Kiel, Germany
[4] Center for Ocean and Society, Kiel University, Kiel, Germany
[5] Istituto Nazionale di Geofisica e Vulcanologia, Etneo, Catania, Italy
[6] Laboratoire Géosciences Ocean, UMR6538 CNRS/University of Brest, Plouzané, France
[7] Department of Geology & Geophysics, University of Aberdeen, Scotland, UK

* Corresponding author : Salvatore Gambino, email address : salvatore.gambino@unict.it

Abstract :

Tectono-stratigraphic interpretation and sequential restoration modelling was performed over two high-resolution seismic profiles crossing the Western Ionian Basin of southern Italy. This analysis was undertaken in order to provide greater insights and a more reliable assessment of the deformation rate affecting the area. Offshore seismic profiling illuminates the sub-seafloor setting where a belt of active normal faults slice across the foot of the Malta Escarpment, a regional-scale structural boundary inherited from the Permo-Triassic palaeotectonic setting. A sequential restoration workflow was established to back-deform the entire investigated sector with the primary aim of analysing the deformation history of the three major normal faults affecting the area. Restoration of the tectono-stratigraphic model reveals how deformation rates evolved through time. In the early stage, the studied area experienced a significant deformation with the horizontal component prevailing over the vertical element. In this context, the three major faults contribute to only one third of the total deformation. The overall throw and extension then notably reduced through time towards the present day and, since the middle Pliocene, ongoing crustal deformation is accommodated almost entirely by the three major normal faults. Unloading and decompaction indicate that when compared to the unrestored seismic sections, a revision and a reduction of roughly one third of the vertical displacement of the faults offset is required. This analysis ultimately allows us to better understand the seismic potential of the region.

Please note that this is an author-produced PDF of an article accepted for publication following peer review. The definitive publisher-authenticated version is available on the publisher Web site.

Highlights

►Sequential restoration has been applied to interpretated high-resolution seismic profiles. ► Back-restoration modelling allows estimating throw-rates of major faults and how it modulated through time. ►data reveal a diffuse stretching in the early deformation stage before strain localized on major faults. ►Sequential restoration workflow allows to reassess deformation rate of a seismically active area of Southern Italy.

Keywords : deformation rate, Malta Escarpment, seismic profile, sequential restoration

Please note that this is an author-produced PDF of an article accepted for publication following peer review. The definitive publisher-authenticated version is available on the publisher Web site.

Acknowledgments

The bathymetric data were extracted from Gutscher et al., (2017) and from EMODnet open dataset (http://www.emodnet-bathymetry.eu/). Digital topographic data are from the Japan Aerospace Exploration Agency (https://www.eorc.jaxa.jp). The authors also acknowledge the use of MOVE Software Suite granted by Petroleum Experts Limited (www.petex.com). This work is part of the S. Gambino's Ph.D. research project at the University of Catania. Bernard Mercier de Lepinay (GeoAzur, Université de Nice/CNRS), is also acknowledged for the CIRCEE-HR seismic data processing.

Funding

This work benefits from founding from the University of Catania in the framework of the project "Multidisciplinary analysis of the deformation around active tectonic structures" (responsible G. Barreca) and partly from the MUSE 4D project - Overtime tectonic, dynamic and rheologic control on destructive multiple seismic events -Special Italian Faults & Earthquakes: from real 4D cases to models in the frame of PRIN 2017.

1. Introduction

The restoration concept includes a wide range of methods (balanced cross-sections, back-stripping, structural restoration etc.), which are applied to validate structural interpretations or to recover deformation, subsidence or any other tectonic processes to be analysed. As seismic data are frequently not associated with well data, application of sequential restoration techniques provides a powerful tool for the validation of structural interpretation (Lopez-Mir et al 2014; Jamaludin et al., 2015; Jitmahantakul et al., 2020), and formulation of kinematic structural models (Suppe, 1983; Suppe and Medwedeff, 1990; Lopez-Mir et al., 2014). Restoration methods are usually based on 'balanced cross sections' as defined by Dahlstrom (1969) and Elliot (1983), which are useful for prediction of geometry at depth (Chamberlin 1910; Bally et al., 1966; Dahlstrom, 1969, 1970; White et al., 1986; Williams and Vann, 1987; Groshong,1990; Wang et al., 2017), and through which all available data are analyzed to ensure that they are geometrically plausible and geologically consistent. These methods usually follow reasonable assumptions about the pre-deformation setting and how rocks behave during deformation in a given tectonic environment (Dahlstrom, 1969).

Since the pioneering studies of Bally et al. (1966) and Dahlstrom (1969), balanced cross sections have been applied to section restoration for validation of structural interpretation and prediction of geometry at depth in both contractional (Hossack, 1979; Boyer and Elliot, 1982; Suppe, 1983; Suppe and Medwedeff, 1990) and extensional settings (Gibbs, 1983-1984; White et al., 1986, Williams and Vann, 1987; Groshong, 1990). More recently, greater computational power has led to a significant acceleration in section modelling and restorations (see Gratier et al., 1991; Egan et al., 1996; Maerten, 2007, among many others). Thanks to such a technological advance, structural balancing and horizon flattening were applied to rectify seismic interpretation in extensional settings (Jamaludin et al., 2015) or to validate 2D seismic interpretation and to calculate extension in various rift phases (Jitmahantakul et al., 2020). Application of the above-mentioned methods represents a powerful approach for basin analysis and for detailing how deformation evolves through time in various tectonic contexts (extensional, compressional or composite).

In this study, sequential restoration methods (see Supplementary Material for description) were applied to analyse the rate of deformation of the extensional Malta Escarpment (hereinafter MESC, see Fig. 1) fault system. The MESC is a former passive margin in the Western Ionian Basin that was reactivated by the Nubia-Eurasia plate convergence during Plio-Quaternary times (Casero et al., 1984; Argnani and Bonazzi, 2005). The reactivation of MESC involved the proximal part of a narrow sedimentary basin in the hanging-wall of the fault system, previously named the 'turbidite valley' (see Gutscher et al., 2016 and Fig.1c), and its recent deformation is expressed by a belt of East-dipping extensional faults slicing across the lower slope of the MESC. Fault activity has led to the development of significant fault-scarps on the seafloor (Bianca et al., 1999; Argnani and Bonazzi, 2002, 2005) that sometimes exceed heights of 60 m (see Gambino et al., 2021). Holocene slip rates estimated by Gambino et al. (2021) for these faults appear atypical when compared with general values recorded in similar tectonic regimes (Galadini and Galli, 2000; Pizzi et al., 2002; Musumeci et al., 2014; Stemberk et al., 2019). Since fault slip rate is an essential parameter in seismotectonic analysis, and considering that the MESC fault system is described by many authors as the seismogenic source for large historical earthquakes in the area (Piatanesi and Tinti, 1998; Bianca et al., 1999; Azzaro and Barbano, 2000; Argnani and Bonazzi, 2005; Argnani et al., 2012), we undertook a sequential restoration work-flow to model the Plio-Quaternary deformation rate of the reactivated northern sector of the MESC fault system. The aim of this work is twofold, a) to reassess fault activity and associated extension and slip rates through-time, and b) to discriminate which kind of processes operate to create basin deformation.

Sequential restoration was performed on a tectono-stratigraphic model developed from the interpretation of two high-resolution seismic profiles that transversally cross the MESC (see Gambino et al.; 2021; Gutscher et al., 2016). After time-to-depth conversion of the seismic profiles (see Gambino et al., 2001), several restoration methods such as sediment unloading and decompaction, isostatic adjustments, erosion restoration, structural restoration and unfolding of the horizons were performed in order to create a geologically consistent sequential restoration (see Supplementary Material). Accordingly, the present-day tectono-stratigraphic model was sequentially restored back to the initial stage of deformation. This approach provides a more reliable estimation of the fault's deformation rate overtime, with significant implications for the seismic hazard of the investigated region.

2. Geological Setting

The 300 km-long Malta Escarpment is located about 20 km offshore Eastern Sicily and separates the thinned/oceanic crust of the Western Ionian Basin from the continental crust of the Pelagian block (Scandone et al., 1981; Fabbri et al., 1982; Casero et al., 1984, Fig.1a). It represents a rifting or spreading-like extensional relict inherited from the Permian-Triassic opening of Neo-Tethys (Şengör, 1979), and the subsequent Mesozoic spreading stage (Ben-Avraham and Grasso, 1991; Catalano et al., 2001). The MESC fault system was reactivated during Quaternary times (Hirn et al., 1997; Bianca et al., 1999; Argnani and Bonazzi, 2005; Palano et al., 2012; Cultrera et al., 2015; Gambino et al., 2021) and is considered one of the most likely sources of major destructive earthquakes in the area over historical times (e.g. the 1169 and 1693 events), even though the actual localization of such events is still controversial (Piatanesi and Tinti, 1998; Bianca et al., 1999; Azzaro and Barbano, 2000; Argnani and Bonazzi, 2005; Argnani et al., 2012; Gambino et al., 2021). This establishes the MESC system as a crucial tectonic feature for the understanding of both the geodynamics of the central Mediterranean and the seismotectonics of the Western Ionian Basin and south-eastern Sicily.

To the East of the MESC, the Ionian Basin (Fig.1a) is interpreted by many authors as a remnant of the Mesozoic Tethys Oceanic crust (Carminati and Doglioni, 2005; Frinzon et al., 2011; Gallais, et al., 2011; Polonia et al., 2017; Speranza et al., 2012; Valenti, 2011), even though the actual nature of the underlying geology is still debated (Dellong et al., 2018). NW-directed subduction of the Ionian oceanic crust beneath the European plate resulted in the development of a large accretionary wedge in the Ionian Sea (the Ionian accretionary wedge or Calabrian accretionary wedge, see Gallais et al., 2012; Polonia et al., 2016). In contrast to the widespread contraction that affects the accretionary wedge, a narrow sector at the western termination of the Ionian Basin (i.e. the turbidite valley, see Gutscher et al., 2016 and Fig.1c for location) has not yet been overthrust by the compressional front of the Ionian Accretionary wedge. Rather, Plio-Quaternary extension is preserved in the area, where the narrow turbidite basin is deformed by a belt of extensional faults that nucleated at the foot of the MESC (F1, F2 and F3 in Fig. 2a; Gambino et al., 2021). Part of this extensional system has been previously reported in the literature (see Hirn et al., 1997; Bianca et al., 1999; Argnani and Bonazzi, 2005; Monaco and Tortorici, 2007; Meschis et al., 2020). The turbidite basin is confined between the MESC to the West, and the compressional front of the Ionian accretionary wedge to the East (Fig.1b). The latter is crosscut to the North by the NW-trending, dextral North Alfeo Fault (NAF in Fig.1b, see Gutscher et al., 2016), which is also known in the literature as the Alfeo-Etna fault (AEF; Polonia et al. 2016, 2017; Sgroi et al. 2021). The AEF accommodates the SE-ward shifting of the Calabria-Peloritani block (Fig.1b), and separates the extensional basin from the contractional domain of the Ionian accretionary wedge (Fig.1b). According to Polonia et al. (2016), the dextral AEF belt includes the Mt. Etna volcano tectonic structures and segments of the MESC that accommodate the tensional component of deformation associated with Africa–Eurasia relative motion.

Submarine canyons excavated in the MESC slope (Micallef et al., 2019, Fig.1c) reveal that the turbidite basin has been filled by both sediments being discharged from the subaerial footwall-block of the Malta Escarpment, and (mainly) the sediments coming from the North, as demonstrated by wave patterns observed in the sedimentary succession within the turbidite basin (Gutscher et al., 2016). Recently, high-resolution seismic surveys in the area (Gutscher et al., 2016) and accurate tectono-stratigraphic interpretation (Gambino et al. 2021), have allowed the active deformation pattern affecting the northernmost sector of the MESC to be redefined. It is characterized by the occurrence of three main, E-dipping fault segments, showing a slight right-lateral component (F1, F2, and F3 in Figs. 1c and 2) mainly distributed along the foot of the MESC bathymetric scarp. According to Gambino et al. (2021), F1 consists of a ~45 km long, two-branched structure, oriented N345E, with a fault surface dipping toward the ENE at ~45°; F2 is a N340E trending two-branched structure, ~35 km-long dipping at 50° toward the ENE; F3 is a 56 km-long segment with a N352E-oriented surface dipping toward the east at 55°. Empirical scaling relationships point to their high seismic potential, especially for F3. Further East, a narrow graben structure, associated with the main fault system, is found to longitudinally deform the turbidite valley, displacing both the section of Quaternary sediments and the seafloor itself (F4, F5 and minor faults in between; Fig.2a).

3. Tectono-stratigraphic model

3.1. Seismic Stratigraphy

The seismic stratigraphy, following Gambino et al. (2021), has been subdivided in four main seismic units (Pre-MES, MES, PQ1, and PQ2) according to well-defined bounding stratigraphic discontinuities (horizons S1, S2, S3 and, seafloor S4, see Fig.2). To better constrain the step-by-step restoration though time, the PQ1 unit has been further subdivided in three sub-units (PQ1a, PQ1b, and PQ1c) according to the detected S3a and S3b bounding unconformities (Fig.2). Since no borehole data are available for the study area, lithologies and ages of the seismic units have been interpreted according to the available literature (see Gambino et al., 2021 and references therein) and summarized in Tab.1. The Pre-MES unit represents the backbone of the Malta Escarpment and has been interpreted as Meso-Cenozoic limestones and marls with sporadic volcanic and/or mud intrusions (Scandone et al., 1981; Catalano et al., 2001; Barreca, 2014). The MES unit has been interpreted as the Messinian sequence based on its seismic characters (high-reflectivity of the top-reflector, see Lofi et al., 2011; Camerlenghi et al., 2019; Micallef et al., 2019 and reference therein) and on its internal seismic facies (Butler et al., 2015). The PQ1 unit (including its subunits PQ1a, PQ1b, and PQ1c) has been interpreted as a Pliocene sedimentary sequence since it correlates with coeval units described by Camerlenghi et al., (2019) and Micallef et al. (2018). According to these authors, the PQ1 subunits are interpreted as sequences of siltstone (shale) and silty-sandstones, calc-lutites and marls, while the PQ2 unit is interpreted as a Quaternary sequence given its seismic character and stratigraphic position. Moreover, its basal erosional surface, dated to 650 ka (Camerlenghi et al., 2019), suggests a correlation with the Middle-late Pleistocene calcarenite sequence outcropping on-land (Servizio Geologico d'Italia, 2011).

Lastly, the interpreted seismic profiles have been Time/Depth converted (as reported in Gambino et al., 2021) using a velocity model (Tab. 1) from the literature (see also Tab.1 in Gambino et al., 2021 and references therein).

3.2. Deformation Pattern

According to Gambino et al. (2021), reactivation of the MESC system is evidenced by an array of seaward-dipping, NNW–SSE trending, extensional faults. The system extends offshore from Catania (Northern termination) to Siracusa (Southern termination) with a total length of ~60 km (Fig.1). The extensional belt includes three main faults (F1, F2, and F3) running close to the MESC lower slope, with a 3.5 km-wide graben structure further to the East bounded by the F4 and F5 faults (Fig. 2a). The F3 structure is the longest fault, reaching a length of ~ 56 km. The activity of the MESC faults has produced a cumulative vertical displacement of the seafloor of about 130 m (see Tab. 2a and b). The offset across faults generally increases with depth involving the entire Plio-Quaternary sequence and the Messinian top reflector (S2, Fig. 2). The estimated rate of fault movement ranges from 0.1 mm/yr during the Pliocene to ~ 0.4 mm/yr during the Pleistocene, with an acceleration of the vertical deformation rate up to 10 mm/yr in the Holocene, measured along the seafloor scarp of the F3 fault (see Gambino et al., 2021). However, this value is probably overestimated and could be the result of various factors affecting bathymetry (erosion, slope instability, etc.).

Farther to the east, the turbidite basin is bounded by a structural high (the so called 'uplifted area' of Argnani and Bonazzi, 2005, Fig. 2a). This has been interpreted as a recent positive flower structure (probably rooted within Messinian unit) resulting from the propagation of the NW-SE trending dextral NAF (see Gutscher et al., 2016 and Fig. 1for location) or, alternatively, as a forced fold produced by the diapiric uprising of mantle-derived serpentinite material (Polonia et al., 2017). The structural culmination is deformed on its shallower portion by a set of high-angle recent and still active faults (Fig. 2a), which have also been considered in the restoration process. The kinematics of these faults is related to the dextral strike-slip nature of NAF (Figs. 1, 2a) that produces a cumulative normal component observed in seismic sections (Cir-01 in Fig.2a).

4. Restoring the model

To back-deform the tectono-stratigraphic model (Fig. 2), a workflow encompassing several restoration methods (i.e. unloading of top units, decompaction of underlying units, isostatic adjustments, erosion restoration, structural restoration and unfolding of horizons), was adopted (see supplementary material). Fault displacement parameters, i.e. throw and extension, have been measured at each restoration cycle. The throw is considered to be the vertical component of the fault offset, independent of the section direction with respect to the fault trend; the extension is considered to be the horizontal component of the fault offset measured along the analysed section. Then, cumulative throw (i.e., sum of the throw values of all faults within the section) and cumulative extension (i.e., the restored horizontal component of each restoration cycle) were reported in Tab. 2a (CIR-01 profile) and Tab. 2b (P607 profile).

4.1. Restoration of the CIR-01 profile

The workflow that was followed to restore the CIR-01 profile involved 48 sequential steps that have included a preliminary tectono-stratigraphic interpretation and a time/depth conversion of seismic units. The most representative steps are shown in Fig.4 where the interpreted CIR-01profile has been restored by applying the proposed restoration workflow (see supplementary material).

After seismic interpretation (Step-01) and time/depth conversion (Step-02), restoration started from the present-day structural configuration (Step-03). At this stage, Block4 is deformed by a graben related to the activity of the F4 and F5 opposite-dipping faults (see Fig. 2) and by other minor faults developed in the uplifted area to the east (see Fig. 2 for details). The graben represents the latest structure to have formed (Gambino et al 2021), since the bounding faults show a constant offset with depth (from PQ1 downward). Indeed, F5 that forms the easternmost fault of the graben (Fig. 2a), shows displacement increasing with depth, indicating its older activity. For this reason, F5 has been restored by several steps that adopt a "simple shear method" (see supplementary material).

In Step-05, the graben has been back-deformed by means of structural restoration applied to both F4 and the minor faults within the graben. In Step-06, the PQ2 unit is back-stripped and the lower units de-compacted accordingly. In Step-07, erosion of PQ1c has been considered in the restoring workflow. To gather information about the amount of eroded succession, the pattern of internal reflectors within the PQ1c unit has been analysed. The seismo-stratigraphic sequences observed in Block1 and Block4b can be considered as lacking erosion since no stratigraphic truncations have been detected. Conversely, parts of the PQ1c are missing in Block2, Block3 and Block 4a (Fig.3a). Accordingly, restoration of the S3 horizon (top of PQc1 unit) is performed by considering the eroded stratigraphic portion and following the geometric pattern of the basal bed of PQ1c unit (the S3a horizon, Fig. 3b). Along Block4a, patterns of internal reflectors indicate significant amounts of erosion with the PQ1c unit locally being only a third of the original stratigraphic thickness. Along Block3, the reflector pattern is difficult to observe due to the chaotic setting, and erosion has been restored by considering the adjacent Blocks 2 and 4.

In Step-12, all the fault offsets are restored with respect to S3 horizon. The constant with depth displacement of faults in the uplifted area (FU2, FU3, FU4, FU5 in Figs. 2a and 4) is restored in one step after the structural restoration of the S3 horizon. This indicates that the onset of faulting occurred after the deposition of the PQ1c unit. At this step, the cumulative extension accommodated by all the faults is ~127 m. In Step-13, unfolding is applied to the S3 horizon. The result is shown in Figs. 3d2 and 4.

In Step-20, the PQ1c is unloaded and lower units de-compacted, while in Step-27, faults are restored with respect to the S3b horizon and a total extension of ~205 m is achieved. In Step-29, all units are unfolded with respect to the S3b horizon. As for Step-13 described above, an inclined and a horizontal datum were adopted for lower-slope and basin units, respectively. It is worth noting that unfolding of the units produced a decoupling (space in Fig. 4) between the lower-slope units (PQ1a, PQ1b and MES) and the Pre-Mes unit. The space reflects the concept of 'area conservation' (Chamberlin, 1910) that is required for 2D restorations. We interpret this feature as being related to accommodation of sediments due to progressive loading. This interpretation could also explain the upward concavity in Step-03 of S3a, S3b, and S3 horizons located on the MESC lower-slope (Fig. 4). Alternatively, the decoupling should be the result of layer-parallel extension, which could have produced volume loss due to an out-of-the-section trending deformation (Bahroudi et al., 2003).

In Step-35, the PQ1b unit is unloaded and lower units de-compacted, while in Step-42, faults are restored with respect to the S3a horizon (top of PQ1a unit). Restoration of the F5 fault led to an inconsistency on the undeformed S2 horizon, which resulted in it being higher in the hanging wall. Even though negligible, such a discrepancy could be the result of an incorrect picking of the S2 horizon.

4.2. Restoration of the P607 profile

The workflow followed for the sequential restoration of the P607 profile involved 19 steps among which the salient ones are shown in Fig. 5. After preparation (interpretation, time-to-depth conversion etc., Steps-01-05) of the seismic profile, the PQ2 unit is unloaded and underlying units de-compacted (Step-06). As for other steps, in the presence of growth strata (see PQ2 unit at Step-05, Fig. 5) sediment unloading and decompaction of lower units follows the operation explained in Fig. 3c (see also supplementary material). Accordingly, different loading on underlying units (located in the footwall and hanging wall, respectively), due to regional and local load (i.e. increased near fault), are unloaded separately.

In Step-08, faults are restored. It is worth noting that, contrary to the CIR-01 profile, no erosional restoration has been performed to the PQ1c unit since the S3 horizon does not provide an indication of the amount of eroded sequence. This is possibly due to a paraconformity that hides the erosional nature of the S3 surface (Fig. 2b). This aspect led to an overestimation of F1 throw (see Fig.6 and section 5).

Unfolding is applied in Step-09. As for the CIR-01 seismic line, an inclined datum was used to unfold units formed on the lower-slope and a horizontal one to unfold units located in the adjacent turbidite basin. In Block2, offset produced by the F2 fault on the S3b horizon (top of the PQ1b unit, see Fig. 3b) is not consistent with the extensional kinematics of the fault, since the footwall is lower than the hanging wall. Moreover, the S3b horizon in Block2 is bent downwards approaching the F2 fault. Since bending is observed neither in the upper nor in the lower horizons, it could be the result of local erosion produced by slope instability. Hence, the S3a horizon has been restored (see below) using the lower S3b horizon as a reference template.

In Step-10, erosion of PQ1b at block2 has been restored (see also Fig. 3b), while in Step-12, the PQ1c unit is unloaded and underlying units de-compacted. Faults are restored in Step-13, and unfolding is applied to the S3b horizon in Step-14. In step-15, the PQ1b unit is unloaded and lower units de-compacted. It is notable that the F2 fault does not produce offset on lower units (PQ1a and MES), suggesting that this fault nucleated after the deposition of the PQ1a unit. In Step-16, faults are restored with respect to the S3a boundary, and in Step-17 unfolding is applied to the S3a horizon. The PQ1a unit has been back-stripped and faults are restored with respect to the S2 horizon in Step-19.

4.3. *Fault displacement parameters and rate of deformation*

The results of the sequential restoration of each seismic profile allowed the investigation of vertical (throw) and horizontal (extension) components of offset experienced by all the faults in the studied sector and their contribution to the overall deformation of the MESC fault system (cumulative throw and restored extension in Tabs. 2a and b for the CIR-01 and the P607 profiles, respectively). For each restoration step, vertical displacement of all faults has been measured (cumulative throw in Tab. 2) and plotted for each displaced unit (Fig. 6). Fault displacement parameters from unrestored seismic sections are also plotted for comparison (Fig. 6a-c). After the restoration process, the measured values of fault throw along the CIR-01 (Fig. 6b) and the P607 (Fig. 6d) profiles show a flattened trend compared to the unrestored sections, marking a significant reduction of the vertical offsets for each displaced horizon. In the CIR-01 profile, a throw reduction is observed for the MESC faults and it progressively increases further back in time. From the PQ1b unit (Middle Pliocene) to the present-day, the MESC faults (F1, F2, and F3) show a relatively flat throw trend with a cumulative throw of about 50 m for each considered horizon (~25 m for the F2 and F3 faults, and ~75 m for the F1 structure, see Tab. 2a and Fig. 6b). The same trend and reduction in offset are observed in the P607 profile except for the PQ1c unit that seems to have experienced up to 250 m of vertical displacement (Fig. 6d). Since the erosional surface at the base of the PQ1c unit is not clearly detectable in the P607 profile, the throw affecting the PQ1c top-horizon (S3 discontinuity) has not been restored relating to the eroded stratigraphic thickness. This limitation probably produced an overestimation of the throw value for the PQ1c unit. Considering that a decrease of about one half of the throw affecting the PQ1c unit was measured in the adjacent CIR-01 profile (Fig. 6b) after restoring the eroded sedimentary thickness, a more reliable throw in the order of ~100 m is inferred for the PQ1c unit also along the P607 profile (see dashed black line in Fig. 6d).

The revised values of fault throw were then used to evaluate the vertical movement of the MESC faults over time (Fig. 7a). During the considered time interval, faults vertically deform the seismic units at an average rate of 0.15 mm/yr (0.18 and 0.14 mm/yr for CIR-01 and P607 profiles respectively, Tab. 3a-b and Fig.7a). The maximum throw-rate value (0.4 mm/yr in the CIR-01) is observed at the Lower-upper-Pliocene transition. During the Upper Pliocene-Pleistocene, throw-rates decrease and stabilize at 0.09 and 0.05 mm/yr for the P607 and CIR-01 profiles, respectively. To discriminate and separate the contribution of the MESC faults to the overall basin deformation (vertical and horizontal components, corresponding to cumulative throw and restored extension, respectively), throw and extension of the MESC extensional system (sum of F1, F2, and F3 components indicated as MESC throw and MESC extension in Tab. 2) have been compared with the total amount of the recovered basin extension (restored extension in Tab. 2) achieved by back-deforming all the faults (Fig. 7b). At the undeformed stage (see step 48 in Fig. 4 and Messinian times in Fig. 7b), restoration of all faults results in ~ 800 m of total horizontal extension and ~640 m of cumulative throw. At this stage, the MESC faults contribute 33% (258 m) of total extension and 39% (251 m) of the achieved cumulative throw (Tab. 3a). Both the vertical and horizontal component of total deformation (blue and red solid lines in Fig. 7b) decrease toward the present-day, roughly correlating with the trend of the deformation components of the MESC faults (see blue and red dashed lines in Fig. 7b). This pattern suggests that in the older stage (MES-PQ1a transition), deformation was rather distributed in most of the faults detected in the tectono-stratigraphic model. The prevalence of the extensional horizontal component provides an insight on this incipient stage of deformation, with a probable diffuse extensional strain across the entire investigated sector. In the mature stage (i.e., moving towards the present-day), almost the entire deformation (i.e., the 97.48% of vertical component, see Tab.3a), is accommodated by the MESC faults, indicating strain localization along these tectonic structures.

5. Discussion

The restoration sequence proposed here aims to better constrain the tectonic rates of faults slicing across the MESC by means of seismo-stratigraphic analysis and restoration modelling. The identification of an erosively truncated unit (the PQ1c top reflector) within the investigated sedimentary section provides additional issues both in applying the restoration workflow and on the estimation of the vertical deformation rate affecting the investigated sector during the Quaternary. Nevertheless, the analysis of the PQ1c/PQ2 erosive truncation (dated at 650 ka, see Camerlenghi et al., 2019) along the CIR-01 profile (Fig.3a) provides an estimation of the amount of erosion experienced by the PQ1c top-reflector (S3 horizon). The reconstruction of the eroded PQ1c unit reveals that up to about one third of its original thickness was eroded (Fig. 3a top-right). The maximum amount of erosion has been inferred at the depocenter of the turbidite basin (70 m, see block 4a in Fig.3a). Such an estimation was not possible in the P607 profile because of the nature of the para-conformity erosive truncation (see Fig. 2b). This issue produced an overestimation of the F1 throw (~250 m) affecting the PQ1c unit. However, according to the restored offset in the adjacent CIR-01 profile, the overestimation was corrected making the fault-throw curve for the P607 (Fig. 6d) consistent with the values of fault throw achieved in the CIR-01 seismic line (Fig.6b). Restoration of the PQ1c original thickness requires a review of previously estimated vertical deformation of the MESC faults during the Quaternary (see Gambino et al., 2021, and Tab. 2a). The F1 restored throw results in about only half of the unrestored one (i.e., from 146.20 m to 69.23 m in the CIR-01 profile see Tab. 2a). Throw along the F2 structure is instead reduced by about one third (from 33.74 to 20.36 m, see Tab. 2a). Negligible reduction in offset is observed for the F3 fault. The different offset reduction along the MESC faults is in line with the higher erosion rate expected along the hanging wall blocks.

Besides the F1 and the F3 tectonic structures, restoration of the F2 fault does not show vertical displacement for the PQ1a and MES units along the P607 profile (red line in Fig. 6d) and for the PQ1a unit along the CIR-01 profile (Fig. 6b). These data suggest that the F2 fault likely nucleated after deposition of the PQ1a unit and hence it is later than the F1 and F3 structures (Lower Pliocene - see Fig. 6d and Step-15 in Fig.5). Sequential restoration allows us to derive information on the fault throw and extension experienced by the entire investigated sector during the considered time-interval. In this context, a throw rate for the MESC faults is calculated considering the age of displaced surfaces in both seismic profiles (Fig. 7a). Since no well data are available, the age of the stratigraphic boundaries could be affected by uncertainties and, accordingly, a reliable estimation of the fault rate becomes rather challenging. The S2 surface (MES top horizon) correlates with the upper Messinian limit and represents the only horizon whose age is well known from literature (5.3 Ma, Camerlenghi et al., 2019; Lofi et al., 2011; Micallef et al., 2019). The PQ1 sediment package is Pliocene in age (see Gambino et al., 2021 and references therein) but uncertainties persist about the ages of its sub-units. Following this limitation, we propose age ranges based on the units' stratigraphic positions (see Tab. 1).

A comparison between the cumulative throw and restored extension (all faults in Cir-01 profile; blue and red solid lines in Fig. 7b) and throw and extension of MESC faults (F1, F2 and F3; blue and red dashed lines in Fig. 7b) provides an insight into how deformation was modulated through time. Plotted values show that throw and extension produced by the activity of the MESC faults (F1, F2, and F3) have comparable values for each restoration step, as expected when the mean dip-angle (45°)

of the faults is taken into account. Throw and extension values maintain roughly constant trends with a slight decrease from the Upper Messinian to the present-day. Conversely, throw and extension values related to the activity of all detected faults (cumulative throw and restored extension) show high values during the Messinian-Lower Pliocene transition. This pattern suggests that in the early stages, extensional deformation was diffuse and probably controlled by all faults. In this time span, MESC faults contributed only ~39% of the total throw and ~33% of the total extension (see the restoration Step-48 in Tab.3a). As deformation continued, cumulative throw and extension decreased and, approaching the present day (PQ2 in Fig. 7b and Tab. 3a), the total throw affecting the area has been largely accommodated by the MESC faults (97.48%). Moreover, in the early deformation stage (from MES to PQ1b in Fig. 7b) restored extension (red solid line) is higher than the total vertical throw (blue solid line) suggesting that horizontal extension was the main component of deformation. Then, from PQ1b onwards, a change in the deformation style is observed with a predominant vertical component. This evidence allowed us to infer that another deformation process, characterized by a major extensional horizontal component, worked simultaneously with the faults' activity in the early stage of deformation. This process is probably related to a diffuse extensional strain developed before fault nucleation or, alternatively, to ductile deformation in the underlying MES unit. It has been suggested that the nature of an underlying detachment layer (frictional or ductile) may play a significant role in developing localised or diffuse faulting in the overlying sedimentary cover (Bahroudi et al., 2003). In this view, the early diffuse deformation observed in fig.7b could be the result of a ductile level in the Messinian unit; with the effect of the ductile level progressively decreasing due to thickness reduction (possibly due to migration out of the section) and faulting localising in to MESC faults.

In the final stage of the CIR-01 restoration (from Step-43 to Step-48 in Fig. 4), the S2 horizon (and related MES unit) remained strongly bent along Block 4. Considering the hyaline nature of the underlying MES unit and that no extensional fault can explain such a bending, the S2 curvature is probably the result of ductile deformation. Lateral escape of the plastic evaporites driven by the increased vertical load is invoked to explain the anomalous bending of the S2 horizon. Salt deformation cannot be restored by means of classical restoration methods since salt typically assumes three-dimensional escape directions and dissolution (Rowan and Ratliff, 2012). Moreover, it is observed how salt migration due to sediment load may produce similar effects of local subsidence and uplift (Rojo et al., 2020), which could explain the non-horizontal attitude of the S2 horizon.

Finally, even if it is not the main object of the work, some considerations can be drawn on the seismogenic potential of the MESC faults: fault dimensions (e.g., for F3), compared to recurrence time interval (see Gambino et al., 2021), are compatible with the magnitudes estimated for large historical earthquakes in the area (e.g., the 1693 and 1169 events) although other seismic sources such as the Alfeo-Etna Fault (Polonia et al., 2016) must be considered as well in the seismotectonic framework of the Western Ionian Basin (see also Gutscher et al., 2016). It is also justified by the acceleration in vertical deformation affecting the MESC faults during the Holocene. Recent extensional reactivation of the MESC faults could be related to tensional component associated with Africa–Eurasia relative motion (Palano et al., 2012) and mostly accommodated by the Alfeo-Etna Fault system, resulting in rifting processes within the Western Lobe of the Calabrian Arc accretionary wedge (see also Polonia et al., 2016).

6. Conclusion

Sequential restoration was applied to a tectono-stratigraphic model derived from the interpretation of two high-resolution seismic profiles crossing the Malta Escarpment and the related extensional basin offshore eastern Sicily. This allowed us to obtain reliable deformation rates for the investigated sector. Sediment unloading/decompaction along with horizon unfolding, and erosional restoration have proven powerful methods in re-interpretation/validation of previously interpreted seismic profiles, and in assessing fault activity and the rate of crustal extension affecting the area.

The main outcomes stemming from this study are summarized as follows:

- Fault displacement parameters derived from the restored seismic profiles indicate that the MESC faults maintain a roughly constant throw (about 150 m, see Fig. 7) for each restoration step. Estimated rates of deformation suggest that the MESC faults throw-rates have been modulated through time spanning from 0.09 to 0.40 mm/yr in the Pliocene, and from 0.05 to 0.09 mm/yr during the Pleistocene. Extensional rates are estimated at 0.06-0.31 mm/yr during the Pliocene, and at 0.03-0.08 mm/yr during the Pleistocene.
- Throw and extension achieved from all faults in the CIR-01 profile indicate that during the early stage (post-Messinian), a diffuse extensional strain affected the investigated sector. This is evidenced by the significant difference between MESC faults deformation (i.e., MESC extension and MESC throw in Fig. 7b) and the cumulative basin deformation (restored cumulative extension and throw in Fig. 7b). In this context, the MESC faults contributed to a third of total horizontal extension and throw during the early deformation stage (Lower Pliocene). As deformation continued, the total deformation (restored cumulative extension and throw in Fig. 7b) decreases and is taken up almost entirely by the MESC faults (Fig.7b). At the present-day, MESC faults accommodate ~97.5% of the total vertical deformation as

well as most of the Quaternary extensional (horizontal) deformation affecting the investigated sector.

- Data analysis also suggests that in the early stages of deformation (MES/PQ1a transition, Fig. 7b), the horizontal component of deformation prevailed over the vertical one. This suggest that another process was active at that time along with the MESC faults, that were probably still in their incipient stage. This extension may be related to ductile deformation within the MES unit.
- Uncertainties persist about the present-day rate of deformation. The high rate of vertical deformation affecting the MESC faults during the Holocene (3-7 mm/yr, see Gambino et al., 2021), is in contrast with the relatively low fault deformation rate (up to 0.4 mm/yr) estimated for the Pliocene sedimentary section. This would imply that a significant acceleration in the (tectonic, non-tectonic?) deformation probably occurred along faults with strain localization and reduction in frictional properties at fault cores.

In conclusion, structural interpretation and sequential restoration along the two analysed high-resolution seismic profiles crossing the Malta Escarpment provide insights that allow us to assess fault deformation rates along this tectonic belt, located in one of the most seismically hazardous areas of the central Mediterranean. Back-deformation of a geologically constrained tectono-stratigraphic model points to a revision of the throw-rates for the MESC faults. The vertical and horizontal deformation rate calculated over time reveals that the investigated sector is a low deforming area. We estimate a more reliable vertical offset that is about 2/3 of that measured in the unrestored sections (e.g., Step-03 for the CIR-01 and Step-05 for the P607 profile, respectively) with significant seismotectonic implications. The workflow presented here allows new insights into basin deformation; in particular, two different processes, which contributed to the tectonic evolution of the basin, have been quantitatively discriminated. Moreover, the workflow has shown itself to be a powerful approach for analysis of basin deformation that can be applied to a wide range of tectonic contexts (extensional, contractional or composite).

References

Airy, G. B. (1855). On the computation of the effect of the attraction of mountain-masses, as disturbing the apparent astronomical latitude of stations of geodetic surveys. Philosophical Transactions of the Royal Society, 145, 101–104.

Amato, A., Azzara, R., Basili, A., Chiarabba, C., Cocco, M., Di Bona, M. & Selvaggi, G. (1995). Main shock and aftershocks of the December 13, 1990, Eastern Sicily earthquake. Annali di Geofisica, vol. 37 (2) p.255-266.

Argnani, A., Armigliato, A., Pagnoni, G., Zaniboni, F., Tinti, S. & Bonazzi, C. (2012). Active tectonics along the submarine slope of south-eastern Sicily and the source of the 11 January 1693 earthquake and tsunami. Nat. Hazards Earth Syst. Sci. 12 (5), 1311–1319. doi:10.5194/nhess-12-1311-2012.

Argnani, A., & Bonazzi, C. (2002). Tectonics of eastern Sicily offshore: preliminary results from the MESC 2001 marine seismic cruise. Boll. Geofis. Teor. Appl. 43 (3–4), 177–193

Argnani, A. & Bonazzi, C. (2005). Malta Escarpment fault zone offshore eastern Sicily: Pliocene-Quaternary tectonic evolution based on new multichannel seismic data. Tectonics 24, TC4009. doi:10.1029/2004TC001656.

Azzaro, R. & Barbano, M.S. (2000). Analysis of the seismicity of southeastern Sicily: a proposed tectonic interpretation. Ann. Geofisc. 43 (1), 171–188. doi:10.4401/ag-3628.

Baldwin, B. & Butler, C.O. (1985). Compaction curves. AAPG Bulletin, 69 (4), 622-626.

Bahroudi A., Koyi, H.A. & Talbot, C.J. (2003). Effect of ductile and frictional décollements on style of extension. Journal of Structural Geology 25, 1401 – 1423.

Bally, A. W., P. L. Gordy, and G. A. Stewart, 1966, Structure, seismic data, and orogenic evolution of southern Canadian Rocky Mountains: Bulletin of Canadian Petroleum Geology, 14, 337–381.

Barnett, J.A.M., Mortimer, J., Rippon, J.H., Walsh, J.J. & Watterson, J. (1987). Displacement geometry in the volume containing a single normal fault. American Association of Petroleum Geologists Bulletin 71 (8): 925-937.

Barreca, G. (2014). Geological and geophysical evidences for mud diapirism in south-eastern Sicily (Italy) and geodynamic implications. J. Geodyn. 82, 168–177. doi:10.1016/j.jog.2014.02.003

Ben-Avraham, Z., and Grasso, M. (1991). Crustal structure variations and transcurrent faulting at the eastern and western margins of the eastern Mediterranean. Tectonophysics 75, 269–277. doi:10.1016/0040-1951(91)90326-N.

Bianca, M., Monaco, C., Tortorici, L. & Cernobori, L. (1999). Quaternary normal faulting in southeastern Sicily (Italy): a seismic source for the 1693 large earthquake. Geophys. J. Int. 139, 370–394. doi:10.1046/j.1365-246x.1999.00942.x

Boyer, S.E. & Elliot, D. (1982). Thrust systems. Bulllet. Am. Assoc. Petrol. Geol. 66, 1196e1230.

Brewer, R. C. & Kenyon, P. M. (1996). Balancing Salt Dome Uplift and Withdrawal Basin Subsidence in Cross-Section. *Journal of StructuralGeology* 18 (4): 493-504. doi:10.1016/0191-8141(95)00098-X

Butler, R.W.H., Lickorish, W.H., Grasso, M., Pedley, H.M. & Ramberti, L. (1995). Tectonics and sequence stratigraphy in Messinian basins, Sicily: Constraints on the initiation and termination of the Mediterranean salinity crisis. Geological Society of America Bulletin, 107(4), 425-439. doi:10.1130/0016-7606(1995)107<0425:TASSIM>2.3.CO;2

Butler, R.W.H., Maniscalco, R., Sturiale, G. & Grasso, M. (2015). Stratigraphic variations control deformation patterns in evaporite basins: Messinian examples, onshore and offshore Sicily (Italy). J. Geol. Soc. 172, 113–124. doi:10.1144/jgs2014-024

Camerlenghi, A., Del Ben, A., Hübscher, C., Forlin, E., Geletti, R., Brancatelli, G., Micallef, A., Saule, M.,& Facchin, L. (2019). Seismic markers of the Messinian salinity crisis in the deep Ionian basin. Basin Research, 32 (4), 716-738. doi:10.1111/bre.12392.

Carminati E. & Doglioni C. (2005): Mediterranean tectonics. In Encyclopedia of Geology, Elsevier, 135-146

Casero, P., Cita, M. B., Croce, M., and De Micheli, A. (1984). Tentativo di interpretazione evolutiva della Scarpata di Malta basata sui dati geologici e geofisici. Mem. Soc. Geol. It. 27, 233–254.

Catalano, R., Doglioni, C. & Merlini, S. (2001). On the Mesozoic Ionian basin. Geophysical Journal International 144(1), 49-64. doi:10.1046/j.0956-540X.2000.01287.x

Catalano, R., Valenti, V., Albanese, C., Accaino, F., Sulli, A., Tinivella, U. et al. (2013). Sicily's fold-thrust belt and slab roll-back: The SI.RI.PRO. seismic crustal transect. Journal of the Geological Society 170(3), 451-464. doi:10.1144/jgs2012-099

Chamberlin, R.T., (1910). The Appalachian folds of central Pennsylvania. The Journal of Geology 18, 228-251.

Chamot-Rooke, N., Rangin, C. & Le Pichon, X. (2005). DOTMED–Deep Offshore Tectonics of the Mediterranean: a synthesis of deep marine data in eastern Mediterranean. Mémoirede la Société géologique de France & American Association of Petroleum Geologists. special number, 177: 64 pp, 9 maps with CD-ROM.

Cultrera, F., Barreca, G., Scarfì, L. & Monaco, C. (2015). Fault reactivation by stress pattern reorganization in the Hyblean foreland domain of SE Sicily (Italy) and seismotectonic implications. Tectonophysics, 661, 215-228, doi: org/10.1016/j.tecto.2015.08.043.

D'Agostino, N., and Selvaggi, G. (2004). Crustal motion along the eurasia-nubia plate boundary in the calabrian arc and sicily and active extension in the messina straits from GPS measurements. J. Geophys. Res. 109, B11402. doi:10.1029/2004JB002998

Dahlstrom, C.D.A. (1969). Balanced cross sections. Canadian Journal of Earth Sciences 6, 743–757.

Dahlstrom, C.D.A., (1970). Balanced cross sections. Can. J. Earth Sci. 18, 332e406.

Dellong, D., Klingelhoefer, F., Kopp, H., Graindorge, D., Margheriti, L., Moretti, M. et al. (2018). Crustal structure of the Ionian basin and eastern Sicily margin: Results froma wide-angle seismic survey. Journal of Geophysical Research: Solid Earth, 123, 2090–2114. https://doi.org/10.1002/2017JB015312

Dickinson, G. (1953). Geological aspects of abnormal reservoir pressures in Gulf Coast, Louisiana: AAPG Bulletin, v. 37, p. 410–432.

Egan, S. S., Buddin, T. S., Kane, S. J., and Williams, G. D., (1997). Three-dimensional modelling and visualization in structural geology: new techniques for the restoration and balancing of volumes, In: Proceedings of the 1996 Geoscience Information Group Conference on Geological Visualisation: Electronic Geology, V. 1, Paper 7, p.67-82.

Egan, S.S., Buddin, T.S., Kane, S.J. & Williams G.D. (1996). Three-dimensional modeling and visualization in structural geology: new techniques for the restoration and balancing of volumes. In: Proceedings of the 1996 Geoscience Information Group Conference on Geological Visualization, Electronic Geology 1, pp. 67–82. Paper 7.

Elliott, D. (1983). The construction of balanced cross sections. Journal of Structural Geology 5, 101.

Fabbri, A., Rossi, S., Sartori, R., and Barone, A. (1982). Evoluzione neogenica dei margini marini dell'Arco Calabro-Peloritano: implicazioni geodinamiche. Mem. Soc. Geol. It. 24, 357–366.

Frizon de Lamotte, D., Raulin, C., Mouchot, N., Wrobel-Daveau, J.C., Blanpied, C. & Ringenbach J.C. (2011). The southernmost margin of the Tethys realm during the Mesozoic and Cenozoic: Initial geometry and timing of the inversion processes. Tectonics 30, TC3002, doi:10.1029/2010TC002691.

Galadini, F. & Galli, P. (2000). Active tectonics in the central Appennines (Italy) - input data for seismic hazard assessment. Natural Hazards, 22(3), 225-268. doi:10.1023/A:1008149531980

Gallais, F., Gutscher, M.A., Graindorge, D., Chamot-Rooke, N. & Klaeschen, D. (2011). A Miocene tectonic inversion in the Ionian Sea (central Mediterranean): evidence from multichannel seismic data. J. Geophys. Res. 116, B12108. doi:10.1029/2011JB008505

Gallais, F., Gutscher, M.A, Klaeschen, D. & Graindorge. D. (2012). Two-Stage Growth of the Calabrian Accretionary Wedge in the Ionian Sea (Central Mediterranean): Constraints from Depth-Migrated Multichannel Seismic Data. Marine Geology 326-328: 28-45. doi:10.1016/j.margeo.2012.08.006

Gambino, S., Barreca G., Gross F., Monaco C., Krastel, S. & Gutscher, MA (2021). Deformation Pattern of the Northern Sector of the Malta Escarpment (Offshore SE Sicily, Italy): Fault Dimension, Slip Prediction, and Seismotectonic Implications. Front. Earth Sci. 8:594176. doi: 10.3389/feart.2020.594176

Ge, H., Jackson, M.P. & Vendeville, B.C. (1997). Kinematics and dynamics of salt tectonics driven by progradation: AAPG Bulletin 81, 398–423.

Gibbs, A.D. (1983). Balanced cross-section construction from seismic sections in areas of extensional tectonics. Journal of Structural Geology 5, 153–160.

Gibbs, A.D. (1984). Structural evolution of extensional basin margins. Journal of the Geological Society, London 141, 609–620.

Gratier, J.P., Guiller, B., Delorme, A. & Odonne, F. (1991). Restoration and balance of a folded and faulted surface by best-fitting of finite elements: principle and applications. Journal of Structural Geology 13, 111–115.

Grenerczy, G., Sella, G., Stein, S., and Kenyeres, A. (2005). Tectonic implications of the GPS velocity field in the northern Adriatic region. Geophys. Res. Lett. 32, L16311. doi:10.1029/2005GL022947

Groshong Jr., R.H. (1990). Unique determination of normal fault shape from hangingwall bed geometry in detached half grabens. Eclogae Geol. Helvetiae 83, 455e471.

Groshong Jr., R.H., Bond, C.E., Gibbs, A., Ratcliff, R. & Wiltschko, D. (2012). Preface: structural balancing at the start of the 21st century: 100 years since Cham-Berlin. J. Struct. Geol. 41, 1e5.

Gross, F., Krastel, S., Geersen, J., Hinrich, B.J., Ridente, D., Chiocci, F. L. et al. (2016). The limits of seaward spreading and slope instability at the continental margin offshore Mt. Etna, imaged by high-resolution 2D seismic data. Tectonophysics 667, 63–76. doi:10.10164/j.tecto.2015.11.011

Gutscher, M.-A., Dominguez, S., Mercier de Lepinay, B., Pinheiro, L., Gallais, F., Babonneau, N., et al. (2016). Tectonic expression of an active slab tear from high-resolution seismic and bathymetric data offshore Sicily (Ionian Sea). Tectonics 35, 39–54. doi:10.1002/2015TC003898

Gutscher, M.-A., Kopp, H., Krastel, S., Bohrmann, G., Garlan, T., Zaragosi, S., et al. (2017). Active tectonics of the Calabrian subduction revealed by new multibeam bathymetric data and high-resolution seismic profiles in the Ionian Sea (Central Mediterranean). Earth Planet Sci. Lett. 461, 61–72. doi:10.1016/j.epsl.2016.12.020

Hirn, A., Nicolich, R., Gallart, J. and the ETNASEIS scientific Group (1997). Roots of Etna Volcano, faults of great earthquakes. Earth and Planetary Science Lett. 148, 171-191.

Hossack, J.R. (1979). The use of balanced cross sections in the calculation of orogenic contraction: a review. J. Geol. Soc. Lond. 136, 705e711.

Jackson, M.P.A., & Talbot, C. J. (1991). A glossary of salt tectonics: Bureau of Economic Geology. Austin, TX: University of Texas at Austin.

Jamaludin, S. N. F., Latiff, A. H. A., & Ghosh, D. P. (2015). Structural balancing vs horizon flattening on seismic data: Example from extensional tectonic setting. Paper presented at the IOP Conference Series: Earth and Environmental Science, , 23(1) doi:10.1088/1755-1315/23/1/012003

Jitmahantakul, S., Phetheet, J., & Kanjanapayont, P. (2020). 2D sequential restoration and basin evolution of the wichianburi sub-basin, phetchabun basin, central thailand. Frontiers in Earth Science, 8 doi:10.3389/feart.2020.578218

Kokinou, E., Vafidis, A., Loucogiannakis, M. & Louis, I. (2013). Deep seismic imaging and velocity estimation in Ionian Sea. J. Balkan Geophys. Soc. 6 (2), 100–116.

Laurent, G., Caumon, G., Bouziat, A., & Jessell, M. (2013). A parametric method to model 3D displacements around faults with volumetric vector fields. Tectonophysics 590, pp.83-93. ff10.1016/j.tecto.2013.01.015ff. ffhal-01301478f

Le Meur, D. (1997). Etude géophysique de la structure profonde et de la tectonique active de la partie occidentale de la Ride Méditerranéenne [Ph.D. thesis]. Paris (FR): University of Paris XI.

Lofi, J., Deverchère, J., Gaullier, V., Gillet, H., Gorini, C., Guennoc, P., et al. (2011). Seismic atlas of the messinian salinity crisis markers in the mediterranean and black seas. Mém. Soc. Géol. CCGM 179, 1–72.

Lopez-Mir, B., Anton Muñoz, J., & García Senz, J. (2014). Restoration of basins driven by extension and salt tectonics: Example from the cotiella basin in the central pyrenees. Journal of Structural Geology, 69(PA), 147-162. doi:10.1016/j.jsg.2014.09.022

Maerten, L., 2007. Geomechanics to solve structure related issues in petroleum reservoirs. AAPG Eur. Reg. Newsl. 2, 2-3.

Maesano, F.E., Tiberti, M.M. & Basili, R. (2017). The Calabrian Arc: three-dimensional modelling of the subduction interface. Sci. Rep. 7, 8887. doi:10.1038/s41598-017-09074-8

Meschis, M., Scicchitano, G., Roberts, G. P., Robertson, J., Barreca, G., Monaco, C., et al., (2020). Regional deformation and offshore crustal local faulting as combined processes to explain uplift through time constrained by investigating differentially uplifted late quaternary paleoshorelines: The foreland hyblean plateau, SE sicily. Tectonics, 39(12) doi:10.1029/2020TC006187

Milia, A., & Torrente, M. M. (2018). Extensional Messinian basins in the Central Mediterranean (Calabria, Italy): new stratigraphic and tectonic insights. Oil & Gas Science and Technology – Revue d'IFP Energies nouvelles, Institut Français du Pétrole 73, pp.45. 10.2516/ogst/2018040. hal-01902842

Micallef, A., Camerlenghi, A., Garcia-Castellanos, D., Cunarro Otero, D., Gutscher, M.-A., Barreca, G., et al., (2018). Evidence of the zanclean megaflood in the eastern mediterranean basin. Scientific Reports, 8(1) doi:10.1038/s41598-018-19446-3

Micallef, A., Camerlenghi, A., Georgiopoulou, A., Garcia-Castellanos, D., Gutscher, M.-A., Lo Iacono, C., et al. (2019). Geomorphic evolution of the Malta Escarpment and implications for the Messinian evaporative drawdown in the eastern Mediterranean Sea. Geomorphology 327, 264–283. doi:10.1016/j.geomorph.2018.11.012

Minelli, L. & Faccenna, C. (2010). Evolution of the Calabrian Accretionary wedge (Central Mediterranean). Tectonics 29 (4), 1-21. http://dx.doi.org/10.1029/2009TC002562

Monaco, C. & Tortorici, L. (2007). Active faulting and related tsunami in eastern Sicily and south-western Calabria. Bollettino di Geofisica Teorica e Applicata 48 (2), 163-184.

Mastrolembo, V. B., Serpelloni, E., Argnani, A., Bonforte, A., Bürgmann, R., Anzidei, M. P., et al. (2014). Fast geodetic strain-rates in eastern sicily (southern Italy): new insights into block tectonics and seismic potential in the area of the great 1693 earthquake. Earth Planet Sci. Lett. 404, 77–88. doi:10.1016/j.epsl.2014.07.025

Musumeci, C., Scarfì, L., Palano, M. & Patanè., D. (2014). Foreland Segmentation Along an Active Convergent Margin: New Constraints in Southeastern Sicily (Italy) from Seismic and Geodetic Observations. Tectonophysics 630 (C), 137-149. doi:10.1016/j.tecto.2014.05.017

Nixon, C.W., Sanderson, D.J., Dee, S.J., Bull, J.M., Humphreys, R.J. & Swanson, M.H. (2014). Fault interactions and reactivation within a normal-fault network at Milne point, Alaska. AAPG Bulletin 98 (10), 2081-2107. doi:10.1306/04301413177

Palano, M., Ferranti, L., Monaco, C., Mattia, M., Aloisi, M., Bruno, V., Cannavò, F.& Siligato, G. (2012). GPS velocity and strain fields in Sicily and southern Calabria, Italy: updated geodetic constraints on tectonic block interaction in the central Mediterranean. J. Geophys. Res. 117, B07401. http://dx.doi.org/10.1029/2012JB009254

Peel, F.J. (2014a). The Engines of Gravity-Driven Movement on Passive Margins: Quantifying the Relative Contribution of Spreading Vs. Gravity Sliding Mechanisms. Tectonophysics 633 (1), 126-142. doi:10.1016/j.tecto.2014.06.023.

Peel, F.J. (2014b). How do Salt Withdrawal Minibasins Form? Insights from Forward Modelling, and Implications for Hydrocarbon Migration. Tectonophysics 630 (C), 222-235. doi:10.1016/j.tecto.2014.05.027.

Piatanesi, A. & Tinti, S. (1998). A revision of the 1693 eastern Sicily earthquake and tsunami. J. Geophys. Res. Solid Earth 103 (B2), 2749–2758. doi:10.1029/97JB03403.

Pizzi, A., Calamita, F., Coltorti, M. & Pieruccini, P. (2002). Quaternary normal faults, intramontane basins and seismicity in the umbria-marche-abruzzi apennine ridge (italy): Contribution of neotectonic analysis to seismic hazard assessment. Bollettino Societa Geologica Italiana 1(2), 923-929.

Polonia, A., Torelli, L., Artoni, A., Carlini, M., Faccenna, C., Ferranti, L., et al. (2016). The Ionian and Alfeo-Etna fault zones: New segments of an evolving plate boundary in the central Mediterranean sea? Tectonophysics 675, 69-90. doi:10.1016/j.tecto.2016.03.016

Polonia, A., Torelli, L., Gasperini, L., Cocchi, L., Muccini, F., Bonatti, E. et al. (2017). Lower plate serpentinite diapirism in the Calabrian arc subduction complex. Nature Communications, 8(1). doi:10.1038/s41467-017-02273-x

Rojo, L.A., Koyi, H., Cardozo, N. & Escalona, A. (2020). Salt tectonics in salt-bearing rift basins: Progradational loading vs extension. Journal of Structural Geology 141 doi:10.1016/j.jsg.2020.104193

Rowan & Ratliff (2012). Cross-section restoration of salt-related deformation: Best practices and potential pitfalls. J. Structural Geol. 41, 24-37.

Scandone, P., Patacca, E., Radoicic, R., Ryan, W. B. F., Cita, M. B., Rawson, M., et al. (1981). Mesozoic and cenozoic rocks from Malta escarpment (Central Mediterranean). AAPG Bull. 65 (7), 1299–1319. doi:10.1306/03B5949F-16D1-11D7-8645000102C1865D.

Schultz-Ela, D.D. (1992). Restoration of cross-sections to constrain deformation processes of extensional terranes. Mar. Petrol. Geol. 9, 372e388.

Sclater, J.G., & Christie, P.A. (1980). Continental stretching: An explanation of the post-Mid-Cretaceous subsidence of the central North Sea Basin. J. Geophysical Res. Solid Earth 85 (B7), 3711-3739.

Şengör, A. M. C. (1979). Mid-mesozoic closure of permo-triassic tethys and its implications. Nature 279, 590-593. doi:10.1038/279590a0

Servizio Geologico d'Italia (2011). Foglio 641 Augusta della Carta Geologica d'Italia alla scala 1:50.000. Coordinatore scientifico Carbone S. Direttore dei rilevamenti Lentini F. Note illustrative a cura di Carbone S. (ISPRA). 247.

Sgroi, T., Polonia, A., Barberi, G., Billi, A., & Gasperini, L. (2021). New seismological data from the calabrian arc reveal arc-orthogonal extension across the subduction zone. Scientific Reports, 11(1) doi:10.1038/s41598-020-79719-8.

Speranza, F., Minelli, L., Pignatelli, A., & Chiappini, M. (2012). The ionian sea: The oldest in situ ocean fragment of the world? Journal of Geophysical Research B: Solid Earth, 117(12) doi:10.1029/2012JB009475.

Stemberk, J., Moro, G.D., Stemberk, J., Blahůt, J., Coubal, M., Košťák, B. et al. (2019). Strain monitoring of active faults in the central apennines (italy) during the period 2002–2017. Tectonophysics 750 22-35. doi:10.1016/j.tecto.2018.10.033

Suppe, J. (1983). Geometry and kinematics of fault-bend folding. Am. J. Sci. 283, 684e721.

Suppe, J., & Medwedeff, D. A. (1990). Geometry and kinematics of fault-propagation folding. Eclogae Geologicae Helvetiae, 83(3), 409-454.

Valenti, V. (2011). New insights from recently migrated CROP multichannel seismic data at the outermost calabrian arc accretionary wedge (ionian sea). Italian Journal of Geosciences, 130(3), 330-342. doi:10.3301/IJG.2011.05

Wang, W., Yin, H., Jia, D., Wu, Z., Wu, C. & Zhou, P. (2017). Calculating detachment depth and dip angle in sedimentary wedges using the area–depth graph. J. Struct. Geol. https://doi.org/10.1016/j.jsg.2017.11.014.

Ward, S. (1994). Constraints on the seismotectonics of the central Mediterranean from very long baseline interferometry. Geophys. J. Int. 117, 441–452. doi:10.1111/j.1365-246X.1994.tb03943.xWhite, N.J., Jackson, J.A., & McKenzie, D.P. (1986). The relationship between the geometry of normal faults and that of sedimentary layers in their hanging walls. J. Struct. Geol. 8, 897e910.

Williams, G., Vann, I., (1987). The geometry of listric normal faults and deformation in their hanging walls. J. Struct. Geol. 9, 789e795.

Figure captions

Fig. 1 - a) Simplified tectonic setting of Sicily and the Western Ionian Basin. HP= Hyblean Plateau; MESC= Malta Escarpment; SFTB= Sicilian Fold and Thrust Belt; CAW=Calabrian Accretionary Wedge. Large blue arrows indicate diverging geodetic velocities (see Ward 1994; Mastrolembo et al., 2014; D'Agostino and Selvaggi, 2004; Grenerczy et al., 2005; Palano et al., 2012) measured in the foreland domain (Hyblean Plateau and Apulia Block) b) Main tectonic structures in the study area with the F1, F2, and F3 faults representing the focus of this work. c) Location of 'turbidite valley' and the analyzed seismic profiles (blue lines). Solid blue lines are the CIR-01 and P607 seismic profiles discussed in the text.

Fig. 2 - Tectono-stratigraphic models used for sequential restoration. a) CIR-01 profile with identification of three main sectors: MESC slope, turbidite basin and uplifted area. The uplifted area corresponds to the North Alfeo Fault system (NAF; Gutscher et al., 2016). b) P607 profile with the MESC slope turbidite basin. For both profiles, the schematic block model (not to scale) used for the restoration process is shown.

Fig. 3 – Main restoration steps. a) Restoration of erosion of the PQ1c unit (CIR-01 profile). Internal reflectors of Block 4b have been considered as the complete seismo-stratigraphic sequence. Accordingly, missing reflectors of Blocks 2, 3 and 4a provide an indication of the amount of erosion. b) Restoration of erosion of the PQ1b unit (P607 profile). S3b horizon (top of PQ1b) shows local erosion (due to slope instability) highlighted by footwall/hangingwall offset. Restoration has been performed using the lower unit top reflector (S3a horizon) as a template. c) Unloading of the upper unit and decompaction of underlying ones. For units showing across-fault thickness variation (growth-strata) we considered a regional load acting on both the footwall and hangingwall of the considered fault, and a local load acting only on the hangingwall. As a result, different decompactions of lower units is applied to the footwall and hangingwall. d) Unfolding of seismic units. Two data have been considered since no paleo-bathymetric datum is available. Datum 2 (which is horizontal in the turbidite basin and inclined on the slope) has been chosen since it is geologically reliable (see text for description).

Fig. 4 – Restoration sequence of CIR-01 profile. Bottom-right represents the present-day setting. In every restoration cycle, structural restoration is performed, and the related amount of extension is reported. At the end of each cycle, the inferred age is reported.

Fig. 5 – Restoration sequence of the P607 profile. The present-day setting is shown in the bottom-right. In every restoration cycle, structural restoration is performed, and the related amount of extension is reported. At the end of each cycle, the inferred age is reported.

Fig. 6 – Throw values measured on tectono-stratigraphic models before (a, c) and after (b, d) restoration. In the time range axis, the measured units are reported. For the restored diagrams (b, d) throw values are measured before the structural restoration steps. When the considered unit represents the top unit of the sequence, the relative step numbers (related to Figs. 4 and 5) are reported above.

Fig. 7 - a) Cumulative throw-rate of F1, F2 and F3 faults (MESC faults) relative to CIR-01 (blue line) and P607 (red line). Every value is relative to the time interval between the seismic units reported

(inferred ages are reported in Tab.1b). Displacement components achieved from the restoration of the CIR-01 profile. Dotted lines are relative to MESC faults parameters (throw and extension respectively blue and red) and solid lines are relative to the cumulative parameters (throw and extension respectively blue and red) of all faults within the seismic profile.

Tab. 1 – Physical parameters attributed to the detected seismic units used for sequential restoration. Ages, lithologies and seismic velocities are based on literature data (see Gambino et al., 2021 and reference therein).

Tab. 2 – Results achieved by means of the sequential restoration process (blue highlighted values are post-calculated). a) Data related to the restoration of the CIR-01 profile; b) Data related to the restoration of the P607 profile.

Tab. 3 – Main results of sequential restoration (values of throw and extension) and data elaboration (rates) of CIR-01 (a) and P607 (b).

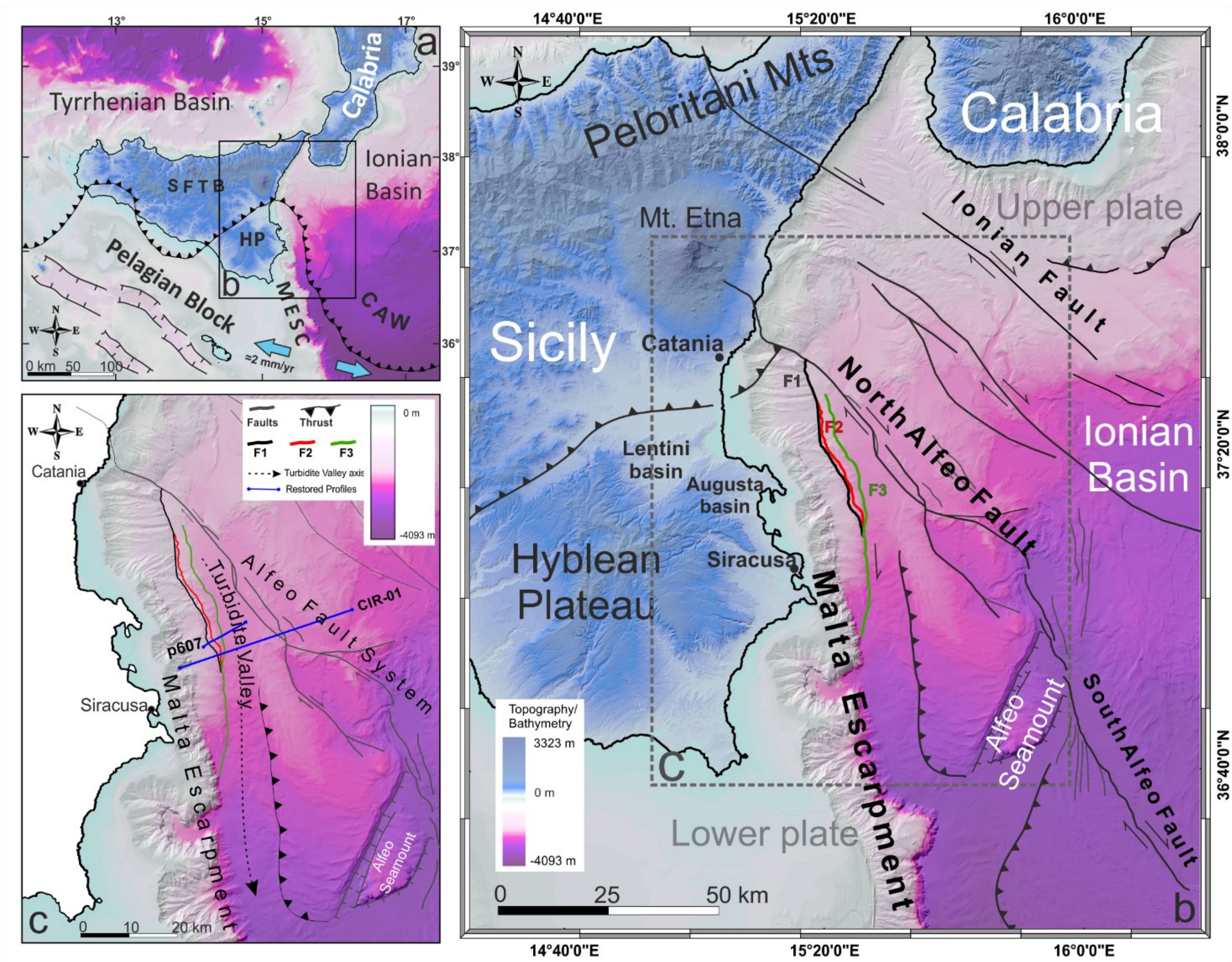

Fig.1

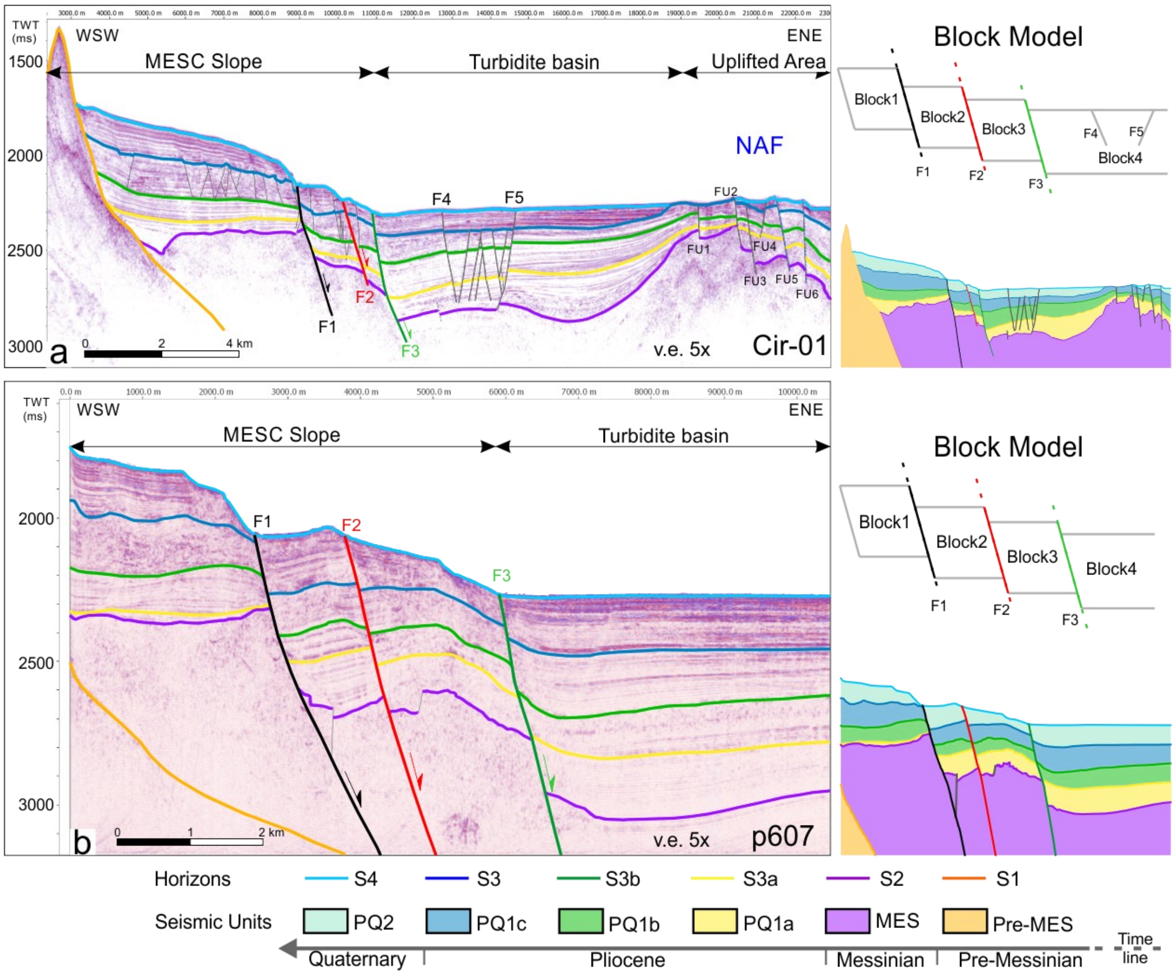
TWT (ms)
WSW
ENE
MESC Slope
Turbidite basin
Uplifted Area
NAF
F1
F2
F3
F4
F5
FU1
FU2
FU3
FU4
FU5
FU6
a
v.e. 5x
Cir-01
Block Model
Block1
Block2
Block3
Block4
MESC Slope
Turbidite basin
b
v.e. 5x
p607
Horizons
S4
S3
S3b
S3a
S2
S1
Seismic Units
PQ2
PQ1c
PQ1b
PQ1a
MES
Pre-MES
Quaternary
Pliocene
Messinian
Pre-Messinian
Time line

Fig.2

792
793
794

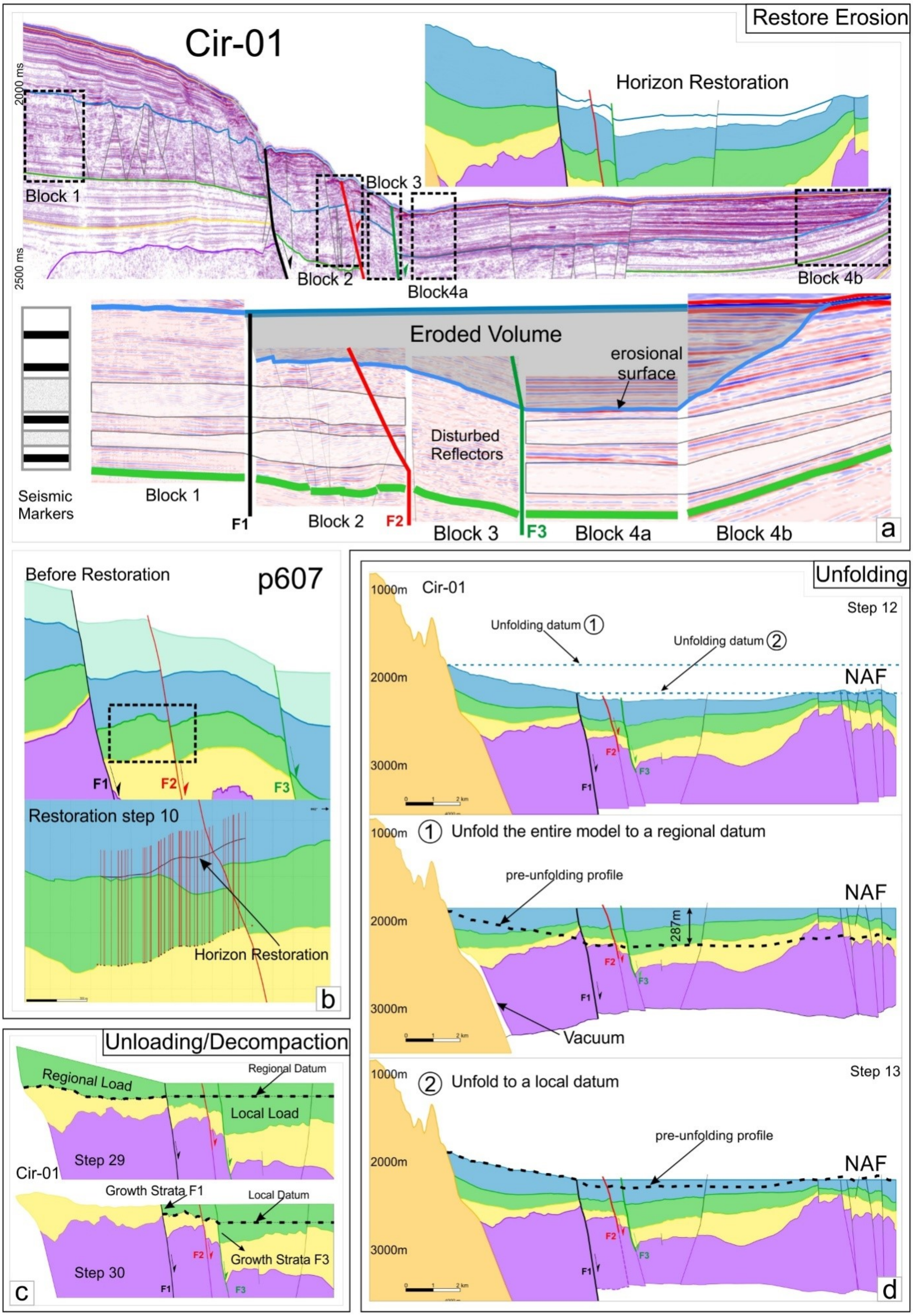

Fig.3

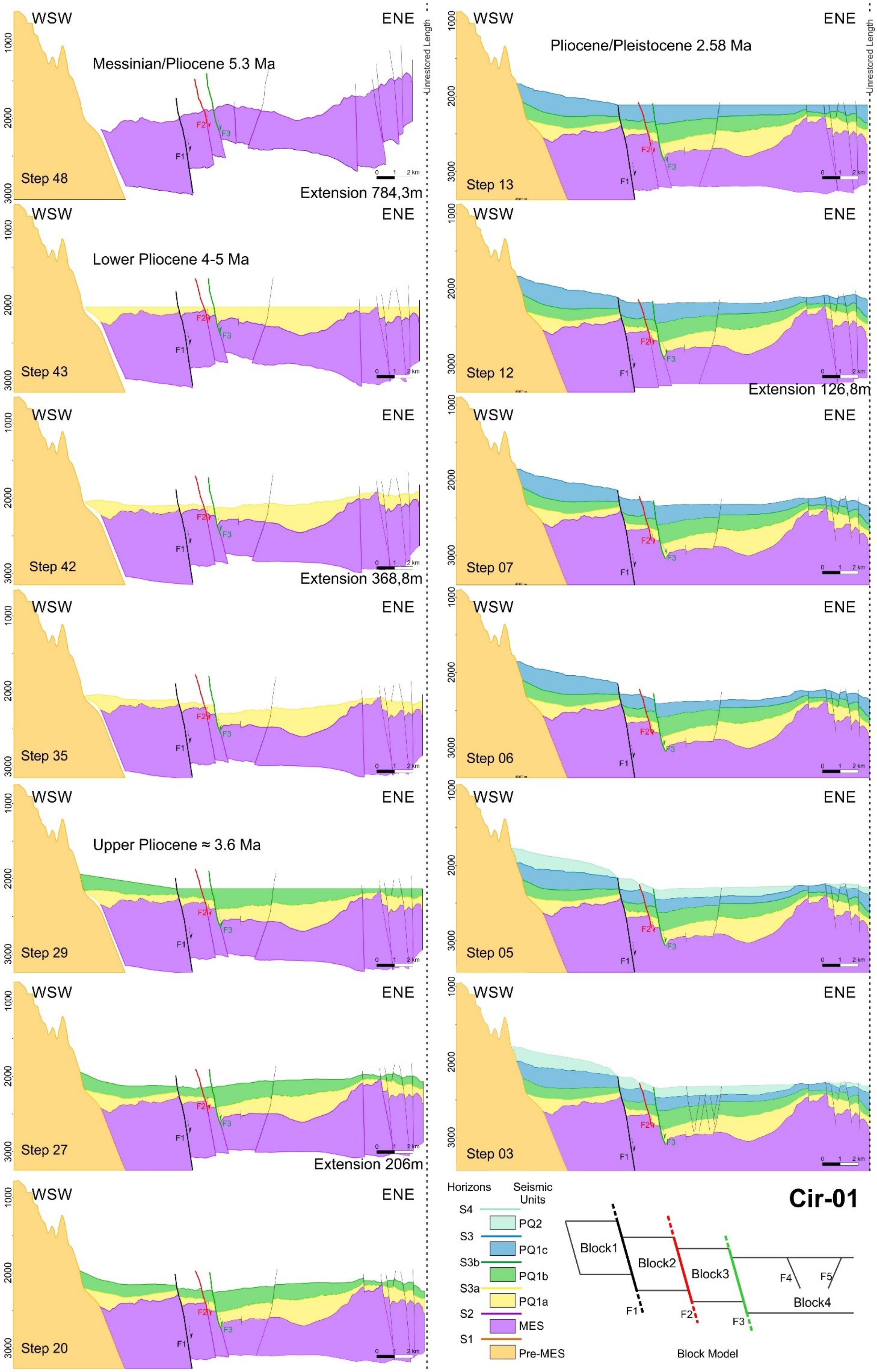
WSW
ENE
Messinian/Pliocene 5.3 Ma
Step 48
Extension 784,3m
Lower Pliocene 4-5 Ma
Step 43
Step 42
Extension 368,8m
Step 35
Upper Pliocene ≈ 3.6 Ma
Step 29
Step 27
Extension 206m
Step 20
Pliocene/Pleistocene 2.58 Ma
Step 13
Step 12
Extension 126,8m
Step 07
Step 06
Step 05
Step 03
Unrestored Length
F1
F2
F3
1000
2000
3000
0 1 2 km
Horizons
Seismic Units
S4
PQ2
S3
PQ1c
S3b
PQ1b
S3a
PQ1a
S2
MES
S1
Pre-MES
Cir-01
Block1
Block2
Block3
Block4
F4
F5
Block Model

Fig.4

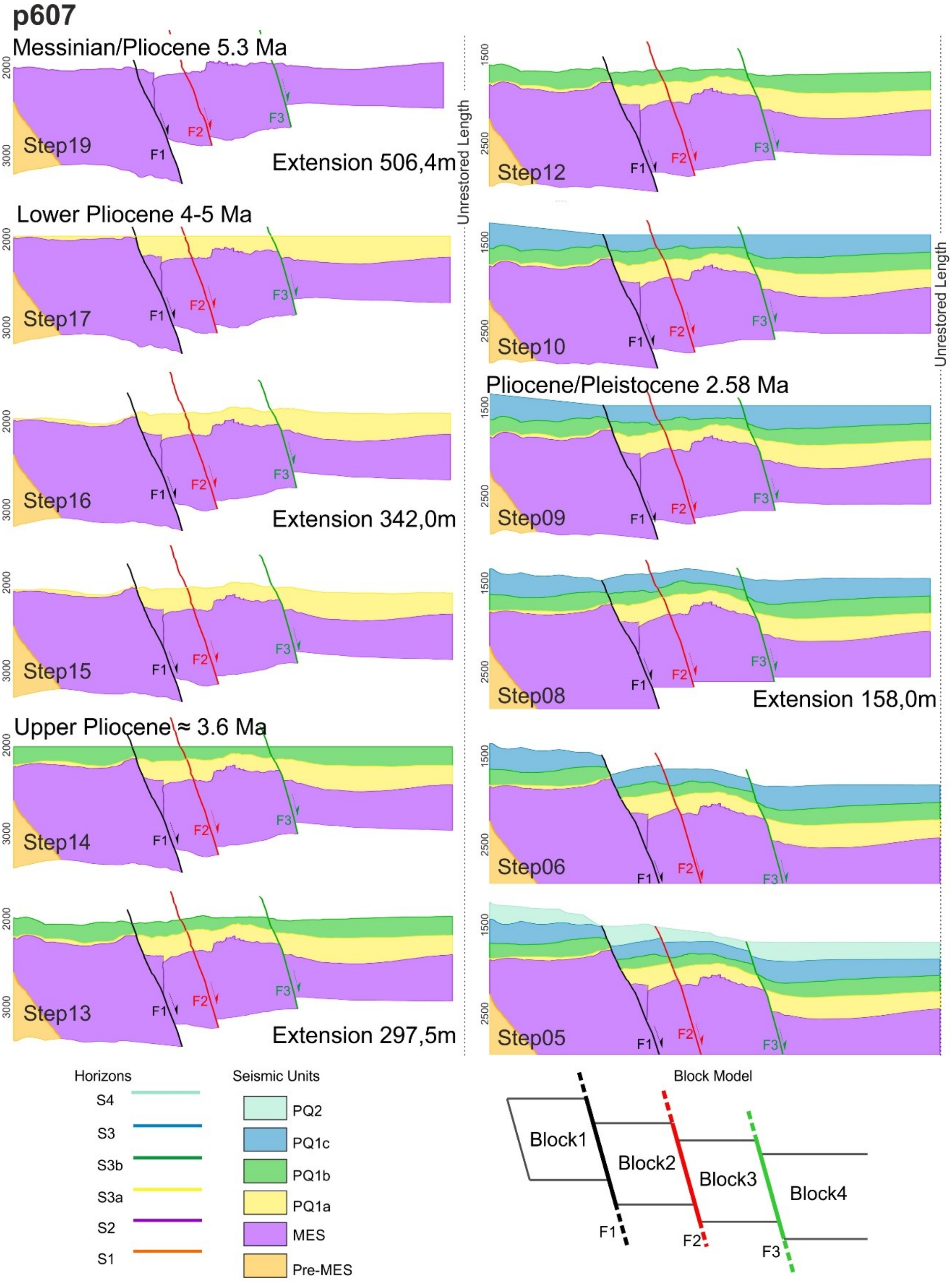
p607
Messinian/Pliocene 5.3 Ma
Step19
Extension 506,4m
Lower Pliocene 4-5 Ma
Step17
Step16
Extension 342,0m
Step15
Upper Pliocene ≈ 3.6 Ma
Step14
Step13
Extension 297,5m
Step12
Step10
Pliocene/Pleistocene 2.58 Ma
Step09
Step08
Extension 158,0m
Step06
Step05
Unrestored Length
F1
F2
F3
2000
3000
1500
2500
Horizons
S4
S3
S3b
S3a
S2
S1
Seismic Units
PQ2
PQ1c
PQ1b
PQ1a
MES
Pre-MES
Block Model
Block1
Block2
Block3
Block4

Fig.5

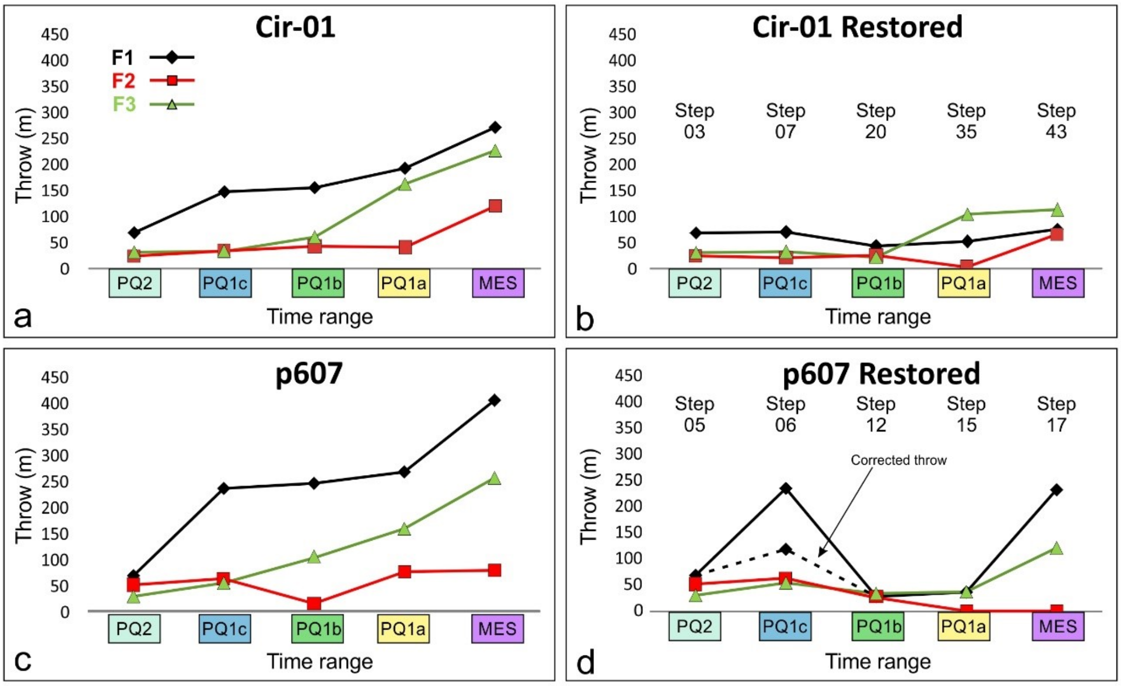
Cir-01
F1
F2
F3
Throw (m)
Time range
PQ2
PQ1c
PQ1b
PQ1a
MES
a
Cir-01 Restored
Step 03
Step 07
Step 20
Step 35
Step 43
b
p607
c
p607 Restored
Step 05
Step 06
Step 12
Step 15
Step 17
Corrected throw
d

Fig.6

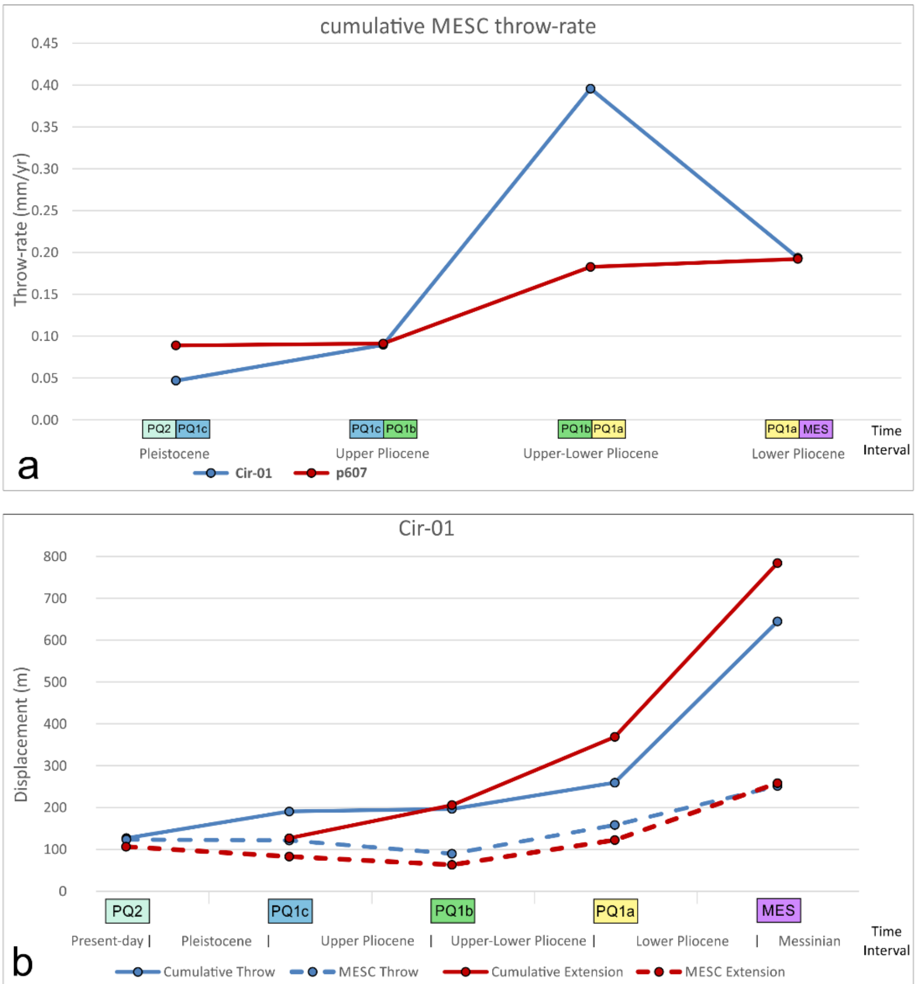
cumulative MESC throw-rate
Throw-rate (mm/yr)
PQ2 PQ1c
Pleistocene
PQ1c PQ1b
Upper Pliocene
PQ1b PQ1a
Upper-Lower Pliocene
PQ1a MES
Lower Pliocene
Time Interval
a
Cir-01
p607
Cir-01
Displacement (m)
PQ2
PQ1c
PQ1b
PQ1a
MES
Present-day
Pleistocene
Upper Pliocene
Upper-Lower Pliocene
Lower Pliocene
Messinian
Time Interval
b
Cumulative Throw
MESC Throw
Cumulative Extension
MESC Extension

Fig.7

Seismic Unit	Age	Age (Ma)	Lithology	SeismicVelocity (m/s)	Surface porosity	Density (km/m^3)	Depth Coeff. (km^{-1})
PQ2	Quaternary	2.58-0.012	Silty-sandstones	1760	0.4	2700	0.39
PQ1c	Upper Pliocene	3.6-2.58	Silty-sandstones	2280	0.4	2700	0.39
PQ1b	Upper/Lower Pliocene	4.0-3.6	Silty-sandstones	2280	0.4	2700	0.39
PQ1a	Lower Pliocene	5.3-4.0	Silty-sandstones	2280	0.4	2700	0.39
MES	Messinian	7.2-5.3	Evaporites	4000	0	2200	0.00
Pre-MES	Pre-Messinian	> 7.2	Limestones	3250	0.7	2700	0.71

Tab 1

Cir-01

Restoration Step	Name	F1			F2			F3			MESC	MESC	Cumulative
		Heave	Slip	Throw	Heave	Slip	Throw	Heave	Slip	Throw	Extension	Throw (m)	Extension (m)
03	PQ2	50.72		68.30	27.40		24.10	26.79		31.40	104.92	123.80	NONE
	PQ1c	77.75	165.66	146.20	54.92	64.57	33.74	16.97	36.97	32.85	149.63	212.79	
	PQ1b	142.26	211.89	153.89	44.59	61.43	42.15	46.93	76.44	60.08	233.78	256.12	
	PQ1a	222.64	295.11	190.95	53.84	67.41	40.38	114.89	198.92	160.94	391.38	392.27	
	MES	283.69	392.69	268.79	109.95	165.89	119.13	282.63	365.62	224.56	676.26	612.48	
07-12	PQ1c	36.63	78.40	69.23	26.27	33.24	20.36	20.22	37.79	31.92	83.12	121.51	126.8
	PQ1b	109.50	168.31	125.34	45.16	63.56	44.61	46.29	77.14	61.47	200.96	231.42	
	PQ1a	222.66	294.86	190.56	48.77	61.59	37.48	117.44	206.65	168.39	388.86	396.43	
	MES	283.69	392.95	268.89	109.93	166.68	120.15	282.63	366.21	225.45	676.25	614.49	
20-27	PQ1b	25.77	49.76	42.54	21.47	32.67	24.58	16.03	27.72	22.61	63.27	89.73	206
	PQ1a	107.87	149.11	101.34	28.66	37.46	24.12	81.40	144.80	118.85	217.94	244.31	
	MES	191.87	255.50	166.65	90.01	133.96	94.37	238.54	317.55	203.68	520.43	464.69	
35-42	PQ1a	56.37	77.67	51.62	3.32	4.38	2.86	62.75	121.74	103.78	122.44	158.27	368.8
	MES	145.92	189.58	120.91	74.41	106.64	71.13	207.08	285.39	190.92	427.41	382.96	
43-48	MES	85.61	114.38	75.77	84.75	109.41	64.32	87.93	142.43	111.52	258.29	251.62	784.3

Tab.2a

p607

Restoration Step	Name	F1			F2			F3			Corrected Heave (m)				Corrected Throw (m)				Cumulative Extension (m)
		Heave	Slip	Throw	Heave	Slip	Throw	Heave	Slip	Throw	F1	F2	F3	Tot	F1	F2	F3	Tot	
05	PQ2	69.89		68.20	38.86		50.40	22.94		29.90	69.89	38.86	22.94	131.69	68.20	50.40	29.90	148.50	NONE
	PQ1c	199.41	310.20	235.63	48.56	78.66	61.84	35.30	65.73	55.39	120.73	48.56	35.30	204.59	117.82	61.84	55.39	235.05	
	PQ1b	210.04	324.84	245.36	11.84	19.52	15.52	71.29	128.89	105.88	210.04	11.84	71.29	293.17	245.36	15.52	105.88	366.77	
	PQ1a	244.09	363.43	267.23	56.84	93.55	74.30	156.50	222.85	158.46	244.09	56.84	156.50	457.43	267.23	74.30	158.46	499.99	
	MES	429.09	593.85	404.69	73.33	106.33	76.92	155.07	300.23	254.85	429.09	73.33	155.07	657.49	404.69	76.92	254.85	736.45	
06-08	PQ1c	199.40	307.37	231.69	48.56	78.26	61.31	35.24	63.99	53.36	118.71	48.56	35.24	202.51	115.84	61.31	53.36	230.52	158
	PQ1b	210.02	327.23	248.34	11.84	20.47	16.70	71.28	134.23	112.14	210.02	11.84	71.28	293.14	248.34	16.70	112.14	377.18	
	PQ1a	244.06	364.90	268.87	56.84	97.10	78.73	156.49	228.19	165.87	244.06	56.84	156.49	457.40	268.87	78.73	165.87	513.47	
	MES	429.05	595.73	407.22	73.33	106.81	77.59	155.11	300.85	255.11	429.05	73.33	155.11	657.49	407.22	77.59	255.11	739.92	
12-13	PQ1b	22.64	38.08	30.53	44.05	51.46	26.18	23.17	41.63	34.55	22.64	44.05	23.17	89.86	30.53	26.18	34.55	91.26	297.5
	PQ1a	47.28	95.55	82.55	15.70	21.81	15.14	72.57	103.59	73.92	47.28	15.70	72.57	135.54	82.55	15.14	73.92	171.61	
	MES	190.18	319.06	254.60	16.31	27.33	21.93	103.64	192.26	159.42	190.18	16.31	103.64	310.13	254.60	21.93	159.42	435.95	
15-16	PQ1a	45.29	58.28	36.56	0.00	0.00	0.00	45.29	58.28	36.56	45.29	0.00	45.29	90.57	36.56	0.00	36.56	73.12	342
	MES	170.75	287.74	229.57	0.00	0.00	0.00	87.86	150.49	119.50	170.75	0.00	87.86	258.61	229.57	0.00	119.50	349.07	
17-19	MES	132.80	228.00	183.50	0.00	0.00	0.00	62.30	91.40	66.40	132.80	0.00	62.30	195.10	183.50	0.00	66.40	249.90	506.4

Tab.2b

Cir-01										
Step	Unit	Cumulative Throw (m)	MESC Throw (m)	% Throw	MESC throw rate (mm/yr)	Cumulative Extension (m)	MESC Extension (m)	% Extension	Total Ext. Rate (mm/yr)	MESC Ext. Rate (mm/yr)
03	PQ2	127.00	123.80	97.48	12.38		104.92			10.49
07 - 12	PQ1c	190.89	121.51	63.65	0.05	126.80	83.12	65.55	0.05	0.03
20 - 27	PQ1b	196.80	89.73	45.59	0.09	206.00	63.27	30.71	0.21	0.06
35 - 42	PQ1a	259.38	158.27	61.02	0.40	368.80	122.44	33.20	0.92	0.31
43 - 48	MES	644.62	251.62	39.03	0.19	784.30	258.29	32.93	0.60	0.20

Tab.3a

p607					
Step	Unit	MESC Throw (m)	MESC Throwrate (m)	MESC Extension (m)	MESC Ext. Rate (mm/yr)
05	PQ2	148.50	14.85	131.69	13.17
06 - 08	PQ1c	230.52	0.09	202.51	0.08
12 - 13	PQ1b	91.26	0.09	89.86	0.09
15 - 16	PQ1a	73.12	0.18	90.57	0.23
17 - 19	MES	249.90	0.19	195.10	0.15

Tab.3b